

Higher Landau-Level Analogs and Signatures of Non-Abelian States in Twisted Bilayer MoTe₂

Chong Wang,^{1,*} Xiao-Wei Zhang,^{1,*} Xiaoyu Liu,¹ Jie Wang,² Ting Cao,^{1,†} and Di Xiao^{1,3,‡}

¹*Department of Materials Science and Engineering, University of Washington, Seattle, WA 98195, USA*

²*Department of Physics, Temple University, Philadelphia, Pennsylvania, 19122, USA*

³*Department of Physics, University of Washington, Seattle, WA 98195, USA*

Recent experimental discovery of fractional Chern insulators at zero magnetic field in moiré superlattices has sparked intense interests in bringing Landau level physics to flat Chern bands. In twisted MoTe₂ bilayers (tMoTe₂), recent theoretical and experimental studies have found three consecutive flat Chern bands at twist angle $\sim 2^\circ$. In this work, we investigate whether higher Landau level physics can be found in these consecutive Chern bands. At twist angles 2.00° and 1.89° , we identify four consecutive $C = 1$ bands for the K valley in tMoTe₂. By constructing Wannier functions directly from density functional theory (DFT) calculations, a six-orbital model is developed to describe the consecutive Chern bands, with the orbitals forming a honeycomb lattice. Exact diagonalization on top of Hartree-Fock calculations are carried out with the Wannier functions. Especially, when the second moiré miniband is half-filled, signatures of non-Abelian states are found. Our Wannier-based approach in modelling moiré superlattices is faithful to DFT wave functions and can serve as benchmarks for continuum models. The possibility of realizing non-Abelian anyons at zero magnetic field also opens up a new pathway for fault-tolerant quantum information processing.

Introduction.—Recent experiments [1–5] and theories [6–12] have identified a series of Abelian fractional Chern insulators (FCI), such as the Laughlin states and other Jain sequence states, as well as gapless composite fermi liquids (CFL), in moiré superlattices at zero magnetic field. The emergence of these exotic states is attributed to the existence of flat Chern bands [13–16] in these systems. Specifically, in twisted homobilayer transition metal dichalcogenides, within the framework of the continuum model, electrons can be viewed as hopping in a layer pseudospin skyrmion lattice, giving rise to topologically nontrivial flat bands [17–19]. The quantum geometry of these flat Chern bands resembling that of the lowest Landau level (LLL) is one of the important reasons for the emergence of the above exotic states [20–27].

More exotic states, such as the Moore-Read (MR) state featuring non-Abelian excitations [28], can be stabilized by Coulomb interaction in the first Landau Level (LL) [29–32]. In a recent density functional theory (DFT) study of twisted bilayer MoTe₂ (tMoTe₂), it is discovered that three consecutive flat bands with Chern numbers equal to 1 appear at twist angle 2.14° for each valley [33], which has not been predicted in the continuum model description within the first harmonic approximation. The existence of three consecutive flat Chern bands has also been corroborated by experimental observations at similar twist angles [34]. These consecutive flat Chern bands with identical Chern numbers bear a striking resemblance to the series of LLs, hinting at the possibility of bringing higher LL physics to moiré superlattices at zero magnetic field, especially the non-Abelian state such as MR.

In this work, we first extend our previous large-scale DFT calculations on tMoTe₂ to additional twist angles near 2° . We identify four consecutive $C = 1$ bands at twist angles 2.00° and 1.89° for the K valley. To accurately describe

the quantum geometry, we construct Wannier functions directly from DFT calculations and develop a six-orbital model to describe the consecutive Chern bands, where the orbitals form a honeycomb lattice. For the second moiré miniband, the integral of the trace of the Fubini-Study metric [$\text{tr}(g)$] is shown to be close to that of the first LL. In addition, the fluctuations of Berry curvature and $\text{tr}(g)$ can be significantly suppressed by band mixing in Hartree-Fock (HF) calculations, enhancing the analogy between the second moiré miniband and the first LL. Exact diagonalization (ED) on top of HF calculations are carried out using the Wannier functions. When the second moiré miniband is half-filled, signatures of non-Abelian states are found. Our Wannier-based approach in modelling the moiré superlattice is faithful to DFT wave functions and can serve as benchmarks for continuum models. The possibility of realizing non-Abelian states in tMoTe₂ also opens up an exciting avenue in realizing higher LL physics in moiré superlattices.

Consecutive Chern bands in tMoTe₂.—When moiré superlattices are formed by twisting two identical monolayers, the original monolayer bands are broken into minibands. For monolayer MoTe₂, the valence band top is located at two corners (K and K') of the honeycomb Brillouin zone. In moiré superlattices, the bands from both K and K' valley form two independent sets of minibands. The two sets of bands are partners under the operation of time reversal symmetry. Our previous large-scale density-functional-theory (DFT) calculations with machine learning force fields has revealed an intricate dependence of the band topology on twist angles [33]. Interestingly, at twist angle of 2.14° , K valley valence bands of tMoTe₂ feature three consecutive Chern bands with $C = 1$. With hole doping, these Chern bands can be revealed in experiments when valleys are spontaneously polarized due to electron-

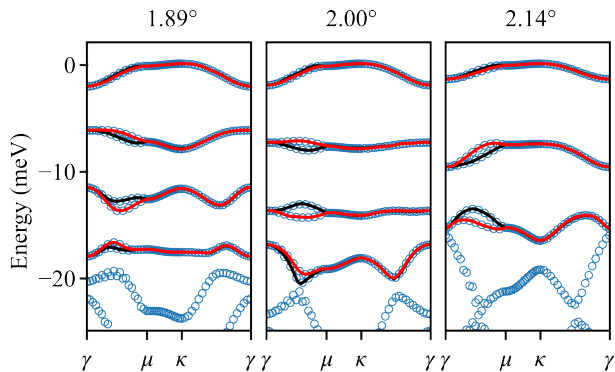


FIG. 1. Bands for tMoTe₂ at twist angles 1.89°, 2.00° and 2.14°. Empty blue circles are from DFT calculations, and solid lines are from Wannier interpolation. For Wannier interpolated bands, red lines are from the K (spin up) valley and black lines are from the K' (spin down) valley. All Wannier interpolated bands have Chern number $C = +1$ for the K valley. Only Wannier interpolated bands in the frozen window are shown here.

electron interactions.

To further explore the band topology of tMoTe₂ around this twist angle, we perform DFT calculations at two other twist angles 2.00° and 1.89°, following the same method introduced in Ref. [33], where the DFT-D2 Van der Waals correction [35] is used [33, 36]. The moiré valence bands from all three angles are shown in Fig. 1. Four consecutive $C = 1$ bands from K valley are found at twist angles 2.00° and 1.89°. At twist angle 2.14°, the fourth band is not well-isolated to have a well-defined Chern number. The Chern numbers are determined by Wannier interpolation with Wannier functions, whose construction will be described below.

The consecutive Chern bands are flat, hinting at the possibility of strong-correlated physics when these bands are partially filled. In this work, we focus on the possibility of realizing first LL physics in tMoTe₂, specifically targeting the second valence band (bands are numbered in the descending order of energy). At the twist angle 2.00°, the second valence band reaches optimal flatness. Therefore, we will focus on this twist angle in the following, deferring the results from other twist angles to Supplemental Material [37].

Quantum geometry from Wannier functions.—To investigate whether consecutive moiré valence bands resemble LL series, accurate modelling is required to capture fluctuations of the quantum geometry of the moiré minibands. Currently, the most common description of moiré superlattice is continuum models, in which the effect of moiré superlattice is described by moiré potentials periodic in the moiré Bravais lattice vectors. However, continuum models fitted to DFT bands within the first few harmonic moiré potentials do not guarantee an accurate reproduction of the quantum geometry [33] such as the Berry curvature Ω and the Fubini-Study metric g from DFT wave functions. Here, we construct Wannier functions to faithfully represent DFT

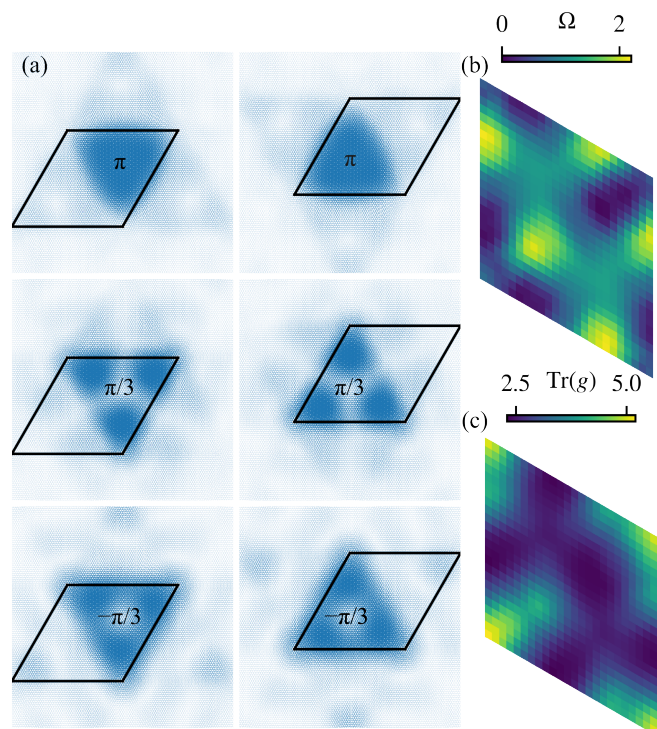


FIG. 2. (a) Real space distributions of the Wannier functions for tMoTe₂ at twist angle 2.00°. Black parallelograms represent moiré unit cell. The phases of the C_3 eigenvalues with respect to the center of the Wannier functions have been labeled. Contributions from both layers have been summed over. (b) and (c) show the distribution of Ω and $\text{tr}(g)$ in the Brillouin zone for the second moiré miniband. The unit for both Ω and $\text{tr}(g)$ is $2\pi/|\Gamma|$, where $|\Gamma|$ is the area of the Brillouin zone. Both Ω and $\text{tr}(g)$ are calculated from the small- \mathbf{q} expansion of the form factors.

wave functions [38] and perform many-body calculations on top of the Wannier functions. The Wannier functions are constructed for the K valley bands, and the K' valley Wannier functions are obtained using time reversal symmetry. The valleys in the DFT calculations are decoupled by distinct Bloch phases and opposite expectation values of the spin- z operator.

Our approach to construct the Wannier functions is the “projection” method [39], which is also the first step in constructing maximally localized Wannier functions [38, 40]. This approach first chooses several trial Wannier functions and then projects the relevant Bloch states onto the trial Wannier functions. The projected Bloch states are subsequently orthogonalized. The Fourier transformation of the orthogonalized projected Bloch states gives the desired Wannier functions. This method generally retains the symmetry properties of the trial Wannier functions [38] and is a powerful tool to construct tight-binding models from DFT calculations.

The DFT bands do not possess a local gap above which the total Chern number is zero. Therefore, band disentanglement [41] needs to be performed to avoid Wannier ob-

struction [42]. A set of frozen states is chosen for which the DFT band energies and Bloch states are faithfully reconstructed. For twist angle 2.14° , we choose the first three valence bands as frozen states. For twist angles 2.00° and 1.89° , first four bands are frozen.

For twist angle 2.00° , the real space plots of the Wannier functions are shown in Fig. 2(a). The Wannier functions form a honeycomb lattice. For each site in the honeycomb lattice, there are three Wannier functions with different three-fold rotation symmetry $[C_3]$ eigenvalues. We have chosen trial Wannier functions centered at MX (Mo on top of Te) and XM (Te on top of Mo) stackings. At some high symmetry \mathbf{k} points, DFT wave functions for certain bands are localized at the MM (Mo on top of Mo) stacking [43], which is covered by linear combinations of the Wannier functions. The Wannier-interpolated bands, along with the DFT bands, are shown in Fig. 1, where an excellent agreement is observed.

In this work, we mainly employ two indicators to compare the quantum geometry of moiré minibands and LLs, namely the trace of the Fubini-Study metric $\text{tr}(g)$ and the Berry curvature. For LLs, the integration of $\text{tr}(g)$

$$\chi = \frac{1}{2\pi} \int_{\text{BZ}} d\mathbf{k} \text{tr}[g(\mathbf{k})] \quad (1)$$

is $2n + 1$, where n is the LL index [44]. With Wannier functions, our calculated results of χ are 1.04, 3.09, 5.11, 7.53 for the topmost four moiré bands, resembling that of LLs. Another important feature of LLs is that they have flat Ω and $\text{tr}(g)$. Targeting the second moiré valence, we plot the distribution of Ω and $\text{tr}(g)$ in the Brillouin zone in Fig. 2(b,c). The fluctuation of Ω and $\text{tr}(g)$ is relatively large, with the standard deviation being 0.51 and 0.67, respectively (Table I). We will show that electron-electron interactions can improve the flatness of Ω and $\text{tr}(g)$ by band mixing.

Coulomb interaction.—To include the electron-electron interactions, we adopt the following interacting Hamiltonian

$$\begin{aligned} \hat{H}_{\text{int}} &= \sum_{\{n\}, \{\mathbf{k}\}, \mathbf{q}} V_{n_1 n_2 n_3 n_4}(\mathbf{k}_1, \mathbf{k}_2, \mathbf{q}) \hat{a}_{n_1 \mathbf{k}_1}^\dagger \hat{a}_{n_2 \mathbf{k}_2}^\dagger \hat{a}_{n_3 \mathbf{k}_2 - \mathbf{q}} \hat{a}_{n_4 \mathbf{k}_1 + \mathbf{q}}, \\ V_{n_1 n_2 n_3 n_4}(\mathbf{k}_1, \mathbf{k}_2, \mathbf{q}) &= \frac{1}{2A} v(\mathbf{q}) f_{n_1 n_4}(\mathbf{k}_1, \mathbf{q}) f_{n_2 n_3}(\mathbf{k}_2, -\mathbf{q}), \end{aligned} \quad (2)$$

where $\hat{a}_{n\mathbf{q}}^\dagger$ creates a Bloch state for band n at crystal momentum \mathbf{q} and A is the area of the system. The summation over \mathbf{k} is in the Brillouin zone and the summation of \mathbf{q} is unbounded. We have taken the convention that the Bloch state is periodic with respect to the reciprocal lattice vectors. We choose the Coulomb interaction screened by symmetric metal gate: $v(\mathbf{q}) = e^2 \tanh(|\mathbf{q}|d)/2\epsilon_0\epsilon|\mathbf{q}|$. Here, e is the elementary charge; d is the distance between tMoTe₂ and the metal gate; ϵ is relative permittivity; ϵ_0 is the vacuum permittivity. The form factor $f_{n_1 n_2}(\mathbf{k}, \mathbf{q})$ is defined as

$$f_{n_1 n_2}(\mathbf{k}, \mathbf{q}) = \langle n_1 \mathbf{k} | e^{-i\mathbf{q}\cdot\mathbf{r}} | n_2 \mathbf{k} + \mathbf{q} \rangle, \quad (3)$$

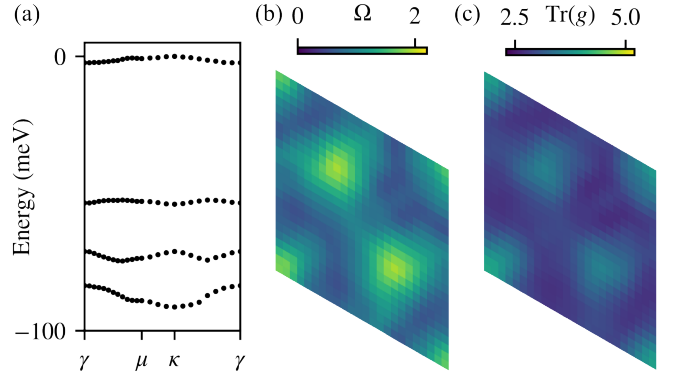


FIG. 3. Hartree-Fock calculations with Wannier functions. (a) shows the Hartree-Fock quasiparticle bands for the K valley. (b) and (c) show the distribution of the Berry curvature Ω and trace of the Fubini-Study metric tensor $\text{tr}(g)$ in the Brillouin zone for the second moiré miniband after HF calculations. The color scale of (b) and (c) is the same as Fig. 2(b,c).

where $|n, \mathbf{k}\rangle$ is a Bloch state. To compute the form factor, we calculate the matrix element $\langle n_1 \mathbf{R}_1 | e^{-i\mathbf{q}\cdot\mathbf{r}} | n_2 \mathbf{R}_2 \rangle$, where $|n\mathbf{R}\rangle$ is the n th Wannier function sitting at the unit cell labeled by the lattice vector \mathbf{R} . $f_{n_1 n_2}(\mathbf{k}, \mathbf{q})$ can then be obtained by a Fourier transformation.

Signatures of non-Abelian states.—One of the most fascinating features in higher LLs is the existence of non-Abelian states such as the MR state. The MR state can be thought of as superconducting paired CFLs [45, 46], and is known to be the exact ground state of a pure three-body short ranged interaction in the LLL [45, 47] or LLL-like Chern bands [48–51], or stabilized by the more realistic Coulomb interaction in the first LL. To explore whether this non-Abelian state can appear in tMoTe₂ at zero magnetic field, ED calculations are required. However, direct ED calculations at doping $\nu = -5/2$ (two and a half holes per moiré unit cell) are prohibitively demanding. Here, we carry out HF calculations at doping $\nu = -2$ to select the active orbitals.

The central object in HF calculations is the one-body reduced density matrix $\rho_{n_1 n_2}(\mathbf{k}_1, \mathbf{k}_2) = \langle \hat{a}_{n_2 \mathbf{k}_2}^\dagger \hat{a}_{n_1 \mathbf{k}_1} \rangle$. For an arbitrary ρ , a mean field decomposition of \hat{H}_{int} gives rise to the HF interaction Hamiltonian $\hat{H}_{\text{HF}}[\rho]$. In DFT calculations, part of the electron-electron interaction has already been taken into account. To avoid double counting, we subtract the $\hat{H}_{\text{HF}}[\rho_0]$ from the total Hamiltonian:

$$\hat{H} = \sum_{n, \mathbf{k}} \epsilon_{n\mathbf{k}} \hat{a}_{n\mathbf{k}}^\dagger \hat{a}_{n\mathbf{k}} + \hat{H}_{\text{int}} - \hat{H}_{\text{HF}}[\rho_0]. \quad (4)$$

Here, $\epsilon_{n\mathbf{k}}$ is the DFT band energy, and ρ_0 is the one-body reduced density matrix from the DFT calculations. HF calculations are carried out with \hat{H} defined above. The subtraction of $\hat{H}_{\text{HF}}[\rho_0]$ ensures that when all valence bands are occupied, the HF calculations reproduce exactly the same band energies and Bloch states from DFT calculations.

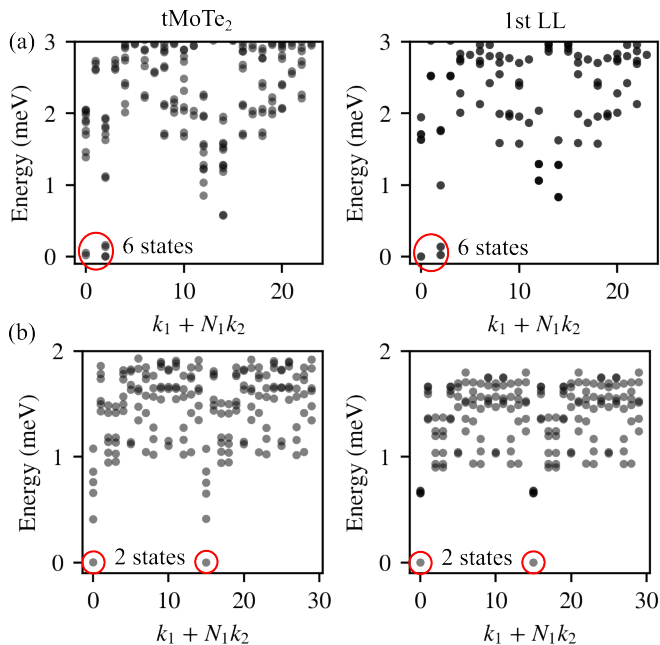


FIG. 4. Many-body spectrum of half-filled second moiré miniband (left) and half-filled first LL (right) on a 4×6 [(a)] and 5×6 [(b)] supercell with periodic boundary condition. The twist angle is 2.00° for tMoTe₂. Parameters: $\epsilon = 5$, $d = 300 \text{ \AA}$.

The results of Hartree-Fock calculations are presented in Fig. 3. Only frozen bands are included in the calculations. An enhanced gap between the first and second moiré valence bands can be observed. Crucially, after HF calculations, the fluctuations of Ω and $\text{tr}(g)$ are significantly reduced by approximately 50% (Table I), while χ slightly decreases (3.09 to 3.02). The improvement of quantum geometry enhances the analogy between the second moiré band and the first LL.

Focusing on the half-filled second moiré valence band, we carry out ED calculations on top of the HF calculations. To avoid double counting of the electron-electron interaction, we again utilize Eq. (4) as the Hamiltonian in ED calculations. In this context, $\epsilon_{n\mathbf{k}}$ and ρ_0 in Eq. (4) are band energies and one-body reduced density matrix from HF calculations. Previously, the double counting removing procedure for HF calculations on top of DFT calculations is heuristic. However, the same procedure, used for ED calculations on top of HF calculations, is exact. The sole purpose of HF calculations is to select relevant Bloch states as single particle orbitals for ED calculations.

On a 4×3 supercell with periodic boundary condition, our ED calculations, restricted to the second moiré valence bands from both valleys, show that fully valley polarized state is the ground state with parameters specified in the caption of Fig. 4. Therefore, we further restrict the ED calculations to the second moiré valence band from the K valley. The many-body spectrums are shown in Fig. 4 for 4×6 and 5×6 supercells with periodic boundary condition. The

TABLE I. Many-body gaps (unit: meV) of non-Abelian state for tMoTe₂ and relevant band properties, including the integration of the quantum metric (χ), the standard deviation of the Berry curvature ($\Delta\Omega$) and the quantum metric [$\Delta\text{tr}(g)$], the band width of the second moiré miniband (w , unit: meV) at various twist angles (θ). NaN indicates that no evidence of non-Abelian states has been found. The gap is identified on a 4×6 supercell and the parameters are the same as that specified in the caption of Fig. 4.

θ	Before HF				After HF				Gap
	χ	$\Delta\Omega$	$\Delta\text{tr}(g)$	w	χ	$\Delta\Omega$	$\Delta\text{tr}(g)$	w	
1.89°	3.07	0.88	0.79	1.80	3.04	0.72	0.59	3.90	NaN
2.00°	3.09	0.51	0.67	0.95	3.02	0.32	0.27	1.59	0.41
2.14°	3.15	0.99	1.08	2.30	3.06	0.28	0.27	1.74	0.11

six-fold and two-fold ground state degeneracy with even and odd number of electrons is the hallmark of the non-Abelian states of MR type or its particle hole conjugate. In Fig. 4, we also show the many-body spectrum of half-filled first LL with Coulomb interaction $v(\mathbf{q}) = e^2/2\epsilon_0\epsilon|\mathbf{q}|$. The LL system is put on the same torus as the corresponding tMoTe₂ system. The number of magnetic fluxes piercing the torus for the LL system is equal to the number of unit cells in the tMoTe₂ system. The striking similarity of the many-body spectrum between tMoTe₂ and the LL system is another strong indication of the non-Abelian states.

In the Supplemental Material [37], we present the many-body spectrum on a 4×6 supercell of half-filled second moiré miniband, but with bare DFT bands. The spectrum bears similarity to that of the half-filled first LL, but lacks the six-fold ground state degeneracy. Therefore, the improved quantum geometry from HF calculations is crucial for the non-Abelian states to appear.

We have also performed calculations for twist angles 1.89° and 2.14° . The quantum geometry before and after HF calculations is presented in Table I. Evidence of non-Abelian states is also found at twist angle 2.14° , but with a smaller many-body gap. No non-Abelian states are found at 1.89° , for which the fluctuations of Ω and $\text{tr}(g)$ are not significantly suppressed by HF calculations.

In LL systems, the MR (Pfaffian) state and its particle-hole (PH) conjugate anti-Pfaffian state are degenerate if LL mixing effects were ignored; the LL mixing provides a PH breaking effect and selects anti-Pfaffian over Pfaffian [52]. Besides Pfaffian and anti-Pfaffian, an intrinsically PH symmetric topological order, PH-Pfaffian, was also proposed [53, 54]. In our systems, the PH symmetry is explicitly broken by the dispersion and non-uniform quantum geometries. We leave more detailed examination of the precise nature of our ground state to the future work, which can be addressed by wave function overlap and entanglement spectrum analysis. Besides $\nu = -5/2$, we also perform ED calculations at other fillings. Specifically, at $\nu = -13/5$, the many-body spectrum for tMoTe₂ also resembles that of the first LL [37], for which the Read-Rezayi

state [55] is supposed to be stabilized.

Compared to FCI states, signatures of non-Abelian states presented here are much weaker. It has been shown that the $\nu = -2/3$ Laughlin state exists in a wide range of twist angles in $t\text{MoTe}_2$ [7, 8]. However, evidences of non-Abelian states are only found in a narrow window of twist angles in this work. In addition, the many-body gap in Fig. 4 is also several times smaller than that of the $\nu = -2/3$ FCI state at the same interaction strength. Finally, our choice of the dielectric constant ϵ gives rise to characteristic interaction strength that is several times larger than the band gap. Therefore, it should be critically evaluated whether the non-Abelian state is stable against band mixing in $t\text{MoTe}_2$, which was proved to be crucial in understanding FCI states in the same system at twist angle around 3.89° [56–58].

We acknowledge useful discussions with Yuchi He, Ying Ran, Lingnan Shen, Kai Sun and Zhao Liu. The exact diagonalization study is supported by DOE Award No. DE-SC0012509. The density-functional theory calculation is supported by the Center on Programmable Quantum Materials, an Energy Frontier Research Center funded by DOE BES under award DE-SC0019443. The machine learning of moiré structure is supported by the discovering AI@UW Initiative and by the National Science Foundation under Award DMR-2308979. This work uses Microsoft Azure credits funded by discovering AI@UW Initiative.

Note added.— We recently became aware of Refs. [59–61]. Ref. [59] proposed the existence of non-Abelian states in free electron gas coupled to Skyrmion lattices. An updated version of Ref. [59] and Refs. [60 and 61] proposed the existence of non-Abelian states in $t\text{MoTe}_2$ based on continuum models fitted to DFT bands. During the referee process, Ref. 62 appeared and introduced the approach of constructing moiré continuum models from DFT bands without fitting. Up to 6 harmonics were included in the continuum model.

* These authors contribute equally to the work.

† tingcao@uw.edu

‡ dixiao@uw.edu

- [1] J. Cai, E. Anderson, C. Wang, X. Zhang, X. Liu, W. Holtzmann, Y. Zhang, F. Fan, T. Taniguchi, K. Watanabe, *et al.*, Signatures of fractional quantum anomalous Hall states in twisted MoTe_2 , *Nature* **622**, 63 (2023).
- [2] H. Park, J. Cai, E. Anderson, Y. Zhang, J. Zhu, X. Liu, C. Wang, W. Holtzmann, C. Hu, Z. Liu, *et al.*, Observation of fractionally quantized anomalous Hall effect, *Nature* **622**, 74 (2023).
- [3] Y. Zeng, Z. Xia, K. Kang, J. Zhu, P. Knüppel, C. Vaswani, K. Watanabe, T. Taniguchi, K. F. Mak, and J. Shan, Thermodynamic evidence of fractional Chern insulator in moiré MoTe_2 , *Nature* **622**, 69 (2023).
- [4] F. Xu, Z. Sun, T. Jia, C. Liu, C. Xu, C. Li, Y. Gu, K. Watanabe, T. Taniguchi, B. Tong, J. Jia, Z. Shi, S. Jiang, Y. Zhang, X. Liu, and T. Li, Observation of integer and fractional quantum anomalous Hall effects in twisted bilayer MoTe_2 , *Phys. Rev. X* **13**, 031037 (2023).
- [5] Z. Lu, T. Han, Y. Yao, A. P. Reddy, J. Yang, J. Seo, K. Watanabe, T. Taniguchi, L. Fu, and L. Ju, Fractional quantum anomalous Hall effect in multilayer graphene, *Nature* **626**, 759 (2024).
- [6] H. Li, U. Kumar, K. Sun, and S.-Z. Lin, Spontaneous fractional Chern insulators in transition metal dichalcogenide moiré superlattices, *Phys. Rev. Res.* **3**, L032070 (2021).
- [7] C. Wang, X.-W. Zhang, X. Liu, Y. He, X. Xu, Y. Ran, T. Cao, and D. Xiao, Fractional Chern insulator in twisted bilayer MoTe_2 , *Phys. Rev. Lett.* **132**, 036501 (2024).
- [8] A. P. Reddy, F. Alsallom, Y. Zhang, T. Devakul, and L. Fu, Fractional quantum anomalous Hall states in twisted bilayer MoTe_2 and WSe_2 , *Phys. Rev. B* **108**, 085117 (2023).
- [9] V. Crépel and L. Fu, Anomalous hall metal and fractional Chern insulator in twisted transition metal dichalcogenides, *Phys. Rev. B* **107**, L201109 (2023).
- [10] N. Morales-Durán, J. Wang, G. R. Schleder, M. Angeli, Z. Zhu, E. Kaxiras, C. Repellin, and J. Cano, Pressure-enhanced fractional Chern insulators along a magic line in moiré transition metal dichalcogenides, *Phys. Rev. Res.* **5**, L032022 (2023).
- [11] J. Dong, J. Wang, P. J. Ledwith, A. Vishwanath, and D. E. Parker, Composite fermi liquid at zero magnetic field in twisted MoTe_2 , *Phys. Rev. Lett.* **131**, 136502 (2023).
- [12] H. Goldman, A. P. Reddy, N. Paul, and L. Fu, Zero-field composite fermi liquid in twisted semiconductor bilayers, *Phys. Rev. Lett.* **131**, 136501 (2023).
- [13] T. Neupert, L. Santos, C. Chamon, and C. Mudry, Fractional Quantum Hall States at Zero Magnetic Field, *Phys. Rev. Lett.* **106**, 236804 (2011).
- [14] E. Tang, J.-W. Mei, and X.-G. Wen, High-Temperature Fractional Quantum Hall States, *Phys. Rev. Lett.* **106**, 236802 (2011).
- [15] D. Sheng, Z.-C. Gu, K. Sun, and L. Sheng, Fractional quantum Hall effect in the absence of Landau levels, *Nat. Commun.* **2**, 389 (2011).
- [16] N. Regnault and B. A. Bernevig, Fractional Chern Insulator, *Phys. Rev. X* **1**, 021014 (2011).
- [17] F. Wu, T. Lovorn, E. Tutuc, I. Martin, and A. MacDonald, Topological Insulators in Twisted Transition Metal Dichalcogenide Homobilayers, *Phys. Rev. Lett.* **122**, 086402 (2019).
- [18] H. Yu, M. Chen, and W. Yao, Giant magnetic field from moiré induced Berry phase in homobilayer semiconductors, *Natl. Sci. Rev.* **7**, 12 (2020).
- [19] N. Morales-Durán, N. Wei, J. Shi, and A. H. MacDonald, Magic angles and fractional chern insulators in twisted homobilayer transition metal dichalcogenides, *Phys. Rev. Lett.* **132**, 096602 (2024).
- [20] S. A. Parameswaran, R. Roy, and S. L. Sondhi, Fractional Chern insulators and the W_∞ algebra, *Phys. Rev. B* **85**, 241308 (2012).
- [21] R. Roy, Band geometry of fractional topological insulators, *Phys. Rev. B* **90**, 165139 (2014).
- [22] B. Mera and T. Ozawa, Kähler geometry and Chern insulators: Relations between topology and the quantum metric, *Phys. Rev. B* **104**, 045104 (2021).
- [23] T. Ozawa and B. Mera, Relations between topology and the quantum metric for Chern insulators, *Phys. Rev. B* **104**, 045103 (2021).
- [24] J. Wang, J. Cano, A. J. Millis, Z. Liu, and B. Yang, Exact Landau level description of geometry and interaction in a flat-band, *Phys. Rev. Lett.* **127**, 246403 (2021).

- [25] P. J. Ledwith, A. Vishwanath, and D. E. Parker, Vortexability: A unifying criterion for ideal fractional Chern insulators, arXiv:2209.15023 (2022).
- [26] J. Wang, S. Klevtsov, and Z. Liu, Origin of model fractional Chern insulators in all topological ideal flatbands: Explicit color-entangled wave function and exact density algebra, Phys. Rev. Res. **5**, 023167 (2023).
- [27] M. Fujimoto, D. E. Parker, J. Dong, E. Khalaf, A. Vishwanath, and P. Ledwith, Higher vortexability: zero field realization of higher Landau levels, arXiv:2403.00856 (2024).
- [28] G. Moore and N. Read, Nonabelions in the fractional quantum Hall effect, Nucl. Phys. B **360**, 362 (1991).
- [29] R. Willett, J. P. Eisenstein, H. L. Störmer, D. C. Tsui, A. C. Gossard, and J. H. English, Observation of an even-denominator quantum number in the fractional quantum Hall effect, Phys. Rev. Lett. **59**, 1776 (1987).
- [30] M. Storni, R. H. Morf, and S. Das Sarma, Fractional quantum Hall state at $\nu = \frac{5}{2}$ and the Moore-Read Pfaffian, Phys. Rev. Lett. **104**, 076803 (2010).
- [31] P. Bonderson, A. Kitaev, and K. Shtengel, Detecting non-abelian statistics in the $\nu = 5/2$ fractional quantum Hall state, Phys. Rev. Lett. **96**, 016803 (2006).
- [32] A. Wójs, G. Möller, S. H. Simon, and N. R. Cooper, Skyrmions in the Moore-Read state at $\nu = \frac{5}{2}$, Phys. Rev. Lett. **104**, 086801 (2010).
- [33] X.-W. Zhang, C. Wang, X. Liu, Y. Fan, T. Cao, and D. Xiao, Polarization-driven band topology evolution in twisted MoTe₂ and WSe₂, Nat. Commun. **15**, 4223 (2024).
- [34] K. Kang, B. Shen, Y. Qiu, Y. Zeng, Z. Xia, K. Watanabe, T. Taniguchi, J. Shan, and K. F. Mak, Evidence of the fractional quantum spin Hall effect in moiré MoTe₂, Nature (2024).
- [35] S. Grimme, Semiempirical GGA-type density functional constructed with a long-range dispersion correction, Journal of computational chemistry **27**, 1787 (2006).
- [36] Y. Jia, J. Yu, J. Liu, J. Herzog-Arbeitman, Z. Qi, H. Pi, N. Regnault, H. Weng, B. A. Bernevig, and Q. Wu, Moiré fractional Chern insulators. I. first-principles calculations and continuum models of twisted bilayer MoTe₂, Phys. Rev. B **109**, 205121 (2024).
- [37] Supplemental Material containing details about construction of Wannier functions, as well as additional many-body spectrums. The Supplemental Material cites Ref. 55, 63, and 64.
- [38] N. Marzari, A. A. Mostofi, J. R. Yates, I. Souza, and D. Vanderbilt, Maximally localized Wannier functions: Theory and applications, Rev. Mod. Phys. **84**, 1419 (2012).
- [39] J. D. Cloizeaux, Energy bands and projection operators in a crystal: Analytic and asymptotic properties, Phys. Rev. **135**, A685 (1964).
- [40] N. Marzari and D. Vanderbilt, Maximally localized generalized Wannier functions for composite energy bands, Phys. Rev. B **56**, 12847 (1997).
- [41] I. Souza, N. Marzari, and D. Vanderbilt, Maximally localized Wannier functions for entangled energy bands, Phys. Rev. B **65**, 035109 (2001).
- [42] C. Brouder, G. Panati, M. Calandra, C. Mourougane, and N. Marzari, Exponential localization of Wannier functions in insulators, Phys. Rev. Lett. **98**, 046402 (2007).
- [43] W.-X. Qiu, B. Li, X.-J. Luo, and F. Wu, Interaction-driven topological phase diagram of twisted bilayer MoTe₂, Phys. Rev. X **13**, 041026 (2023).
- [44] Z. Liu, B. Mera, M. Fujimoto, T. Ozawa, and J. Wang, Theory of generalized Landau levels and implication for non-Abelian states, arXiv preprint arXiv:2405.14479 (2024).
- [45] M. Greiter, X.-G. Wen, and F. Wilczek, Paired Hall states, Nucl. Phys. B **374**, 567 (1992).
- [46] N. Read and D. Green, Paired states of fermions in two dimensions with breaking of parity and time-reversal symmetries and the fractional quantum Hall effect, Phys. Rev. B **61**, 10267 (2000).
- [47] A. Wójs, C. Töke, and J. K. Jain, Global phase diagram of the fractional quantum hall effect arising from repulsive three-body interactions, Phys. Rev. Lett. **105**, 196801 (2010).
- [48] Y.-L. Wu, B. A. Bernevig, and N. Regnault, Zoology of fractional chern insulators, Phys. Rev. B **85**, 075116 (2012).
- [49] Y.-F. Wang, H. Yao, Z.-C. Gu, C.-D. Gong, and D. N. Sheng, Non-abelian quantum hall effect in topological flat bands, Phys. Rev. Lett. **108**, 126805 (2012).
- [50] B. A. Bernevig and N. Regnault, Emergent many-body translational symmetries of abelian and non-abelian fractionally filled topological insulators, Phys. Rev. B **85**, 075128 (2012).
- [51] L. Zhang and X.-Y. Song, Moore-read state in half-filled moiré Chern band from three-body pseudo-potential, arXiv:2403.11478 (2024).
- [52] E. H. Rezayi, Landau level mixing and the ground state of the $\nu = 5/2$ quantum Hall effect, Phys. Rev. Lett. **119**, 026801 (2017).
- [53] X. Chen, L. Fidkowski, and A. Vishwanath, Symmetry enforced non-abelian topological order at the surface of a topological insulator, Phys. Rev. B **89**, 165132 (2014).
- [54] D. T. Son, Is the composite fermion a Dirac particle?, Phys. Rev. X **5**, 031027 (2015).
- [55] N. Read and E. Rezayi, Beyond paired quantum Hall states: Parafermions and incompressible states in the first excited Landau level, Phys. Rev. B **59**, 8084 (1999).
- [56] J. Yu, J. Herzog-Arbeitman, M. Wang, O. Vafek, B. A. Bernevig, and N. Regnault, Fractional Chern insulators versus nonmagnetic states in twisted bilayer MoTe₂, Phys. Rev. B **109**, 045147 (2024).
- [57] C. Xu, J. Li, Y. Xu, Z. Bi, and Y. Zhang, Maximally localized Wannier functions, interaction models, and fractional quantum anomalous Hall effect in twisted bilayer MoTe₂, Proc. Natl. Acad. Sci. U.S.A. **121**, e2316749121 (2024).
- [58] A. Abouelkomsan, A. P. Reddy, L. Fu, and E. J. Bergholtz, Band mixing in the quantum anomalous Hall regime of twisted semiconductor bilayers, Physical Review B **109**, L121107 (2024).
- [59] A. P. Reddy, N. Paul, A. Abouelkomsan, and L. Fu, Non-Abelian fractionalization in topological minibands, arXiv:2403.00059 (2024).
- [60] C. Xu, N. Mao, T. Zeng, and Y. Zhang, Multiple Chern bands in twisted MoTe₂ and possible non-Abelian states, arXiv:2403.17003 (2024).
- [61] C.-E. Ahn, W. Lee, K. Yananose, Y. Kim, and G. Y. Cho, First Landau level physics in second moiré band of 2.1° twisted bilayer MoTe₂, arXiv:2403.19155 (2024).
- [62] Y. Zhang, H. Pi, J. Liu, W. Miao, Z. Qi, N. Regnault, H. Weng, X. Dai, B. A. Bernevig, Q. Wu, *et al.*, Universal moiré-model-building method without fitting: Application to twisted MoTe₂ and WSe₂, arXiv preprint arXiv:2411.08108 (2024).
- [63] L. Chen, T. Mazaheri, A. Seidel, and X. Tang, The impossibility of exactly flat non-trivial Chern bands in strictly local periodic tight binding models, J. Phys. A **47**, 152001 (2014).
- [64] Z. Papić and D. A. Abanin, Topological phases in the zeroth Landau level of bilayer graphene, Phys. Rev. Lett. **112**, 046602 (2014).

Supplemental Material for “Higher Landau-Level Analogs and Signatures of Non-Abelian States in Twisted Bilayer MoTe₂”

Chong Wang,^{1,*} Xiao-Wei Zhang,^{1,*} Xiaoyu Liu,¹ Jie Wang,² Ting Cao,^{1,†} and Di Xiao^{1,3,‡}

¹Department of Materials Science and Engineering, University of Washington, Seattle, WA 98195, USA

²Department of Physics, Temple University, Philadelphia, Pennsylvania, 19122, USA

³Department of Physics, University of Washington, Seattle, WA 98195, USA

I. DETAILS ON WANNIER FUNCTION CONSTRUCTION

The common choices of the trial Wannier functions are atomic orbitals. However, for the purpose of describing moiré minibands, moiré-scale Wannier functions are needed. In this work, we choose the trial Wannier functions to be Bloch states at high symmetric \mathbf{k} points, with a cutoff in real space around high symmetric stackings. There are three high symmetric stackings in tMoTe₂, namely the MX (Mo on top of Te), XM (Te on top of Mo) and MM (Mo on top of Mo) stackings. At some high symmetry \mathbf{k} points, DFT wave functions for certain bands are localized at the MM stacking, prompting the adoption of orbitals at MM stacking in some literature. However, we find it more convenient to choose trial Wannier functions localized at the MX and XM stackings. The Wannier functions constructed are relatively extended and can reproduce the DFT wave function at the MM stacking. We note that due to the existence of flat Chern bands, the Wannier function is required to be relatively extended [1], and our decision of not choosing orbitals at the MM stacking does not significantly increase the size of the Wannier functions.

The six trial Wannier functions are constructed from bands {3, 3, 4, 4, 5, 5}, from \mathbf{k} -points $\{\kappa', \kappa, \kappa', \kappa, \kappa', \kappa\}$, centered at MX, XM, MX, XM, MX, XM stackings, respectively. The real space cutoff is one third of the lattice constant. One example of the Bloch states and the trial Wannier functions are shown in Fig. S1.

II. DETAILS ON CALCULATING FORM FACTORS OF WANNIER INTERPOLATION

The core component to compute form factors for Bloch states is $\langle w_n | e^{i\mathbf{q}\cdot\mathbf{r}} | w_m \rangle$, where $|w_n\rangle$ is the n th Wannier function. The Wannier functions are in turn linear combinations of local orbitals:

$$|w_n\rangle = \sum_{\tau} \sum_{i \in \mathbb{O}_{\tau}} c_{i\tau n} |\tau i\rangle, \quad (\text{S1})$$

Local orbitals are classified according to atoms, which are labeled by their positions τ . The list of orbitals for the atom sitting at τ is denoted as \mathbb{O}_{τ} . Therefore,

$$\langle w_n | e^{i\mathbf{q}\cdot\mathbf{r}} | w_m \rangle = \sum_{\{\tau\}} \sum_{\{i_{\alpha} \in \mathbb{O}_{\tau_{\alpha}}\}} c_{i_1\tau_1 n}^* c_{i_2\tau_2 m} \langle \tau_1 i_1 | e^{i\mathbf{q}\cdot\mathbf{r}} | \tau_2 i_2 \rangle. \quad (\text{S2})$$

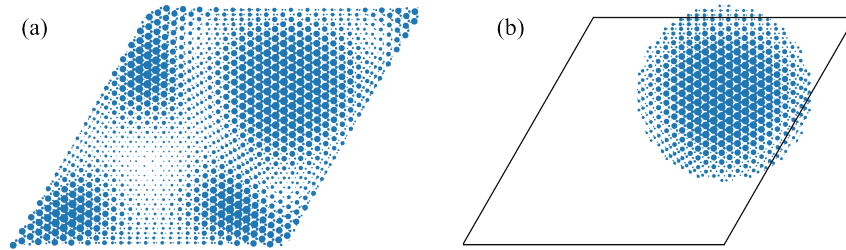


FIG. S1. (a) Real space plot of the Bloch state for the third moiré miniband at κ' point for tMoTe₂ at twist angle 2.00°. (b) The trial Wannier function constructed from the Bloch state in (a).

* These authors contribute equally to the work.

† tingcao@uw.edu

‡ dixiao@uw.edu

We now make the approximation that $\langle \tau_1 i_1 | e^{i\mathbf{q}\cdot\mathbf{r}} | \tau_2 i_2 \rangle \neq 0$ only when $\tau_1 \neq \tau_2$. As a result

$$\langle w_n | e^{i\mathbf{q}\cdot\mathbf{r}} | w_m \rangle \approx \sum_{\tau} \sum_{\{i_{\alpha} \in \mathbb{O}_{\tau}\}} c_{i_1 \tau n}^* c_{i_2 \tau m} \langle \tau i_1 | e^{i\mathbf{q}\cdot\mathbf{r}} | \tau i_2 \rangle \quad (\text{S3})$$

$$= \sum_{\tau} \sum_{\{i_{\alpha} \in \mathbb{O}_{\tau}\}} c_{i_1 \tau n}^* c_{i_2 \tau m} e^{i\mathbf{q}\cdot\tau} \langle \tau i_1 | e^{i\mathbf{q}\cdot(\mathbf{r}-\tau)} | \tau i_2 \rangle. \quad (\text{S4})$$

Here, $\langle \tau i_1 | e^{i\mathbf{q}\cdot(\mathbf{r}-\tau)} | \tau i_2 \rangle$ only depends on τ through the type of atom sitting at τ .

To carry out many-body calculations, it is necessary to introduce a cutoff for \mathbf{q} , since otherwise the summation would be infinite. We assume that $c_{i\tau n}$ varies slowly in space, and therefore only small \mathbf{q} will give rise to significant $\langle w_n | e^{i\mathbf{q}\cdot\mathbf{r}} | w_m \rangle$, introducing a natural cutoff for \mathbf{q} . It is possible to further approximate

$$\langle \tau i_1 | e^{i\mathbf{q}\cdot(\mathbf{r}-\tau)} | \tau i_2 \rangle \approx \langle \tau i_1 | \tau i_2 \rangle \quad (\text{S5})$$

for small \mathbf{q} to simply reuse the overlap matrix from other calculations.

III. DETAILS ON DOUBLE COUNTING REMOVAL PROCEDURE

We start with a general interacting Hamiltonian

$$H = \sum_{\alpha, \beta} T_{\alpha\beta} \hat{c}_{\alpha}^{\dagger} \hat{c}_{\beta} + \frac{1}{2} \sum_{\alpha, \beta, \gamma, \delta} V_{\alpha\beta\gamma\delta} \hat{c}_{\alpha}^{\dagger} \hat{c}_{\beta}^{\dagger} \hat{c}_{\gamma} \hat{c}_{\delta}, \quad (\text{S6})$$

where $V_{\alpha\beta\gamma\delta} = V_{\beta\alpha\delta\gamma}$ is assumed. Here, the single particle basis $\{\alpha\}$ is supposed to be from Hartree-Fock calculations. The Hartree-Fock Hamiltonian is generally

$$H_{\text{HF}} = \sum_{\alpha, \beta} T_{\alpha\beta} \hat{c}_{\alpha}^{\dagger} \hat{c}_{\beta} + \sum_{\alpha, \beta, \gamma, \delta} V_{\alpha\beta\gamma\delta} \left[\langle \hat{c}_{\alpha}^{\dagger} \hat{c}_{\delta} \rangle \hat{c}_{\beta}^{\dagger} \hat{c}_{\gamma} - \langle \hat{c}_{\alpha}^{\dagger} \hat{c}_{\gamma} \rangle \hat{c}_{\beta}^{\dagger} \hat{c}_{\delta} \right], \quad (\text{S7})$$

but since $\{\alpha\}$ are eigenstates, H_{HF} is diagonal

$$T_{\alpha\beta} + \sum_{\gamma} n_{\gamma} (V_{\gamma\alpha\beta\gamma} - V_{\gamma\alpha\gamma\beta}) = \varepsilon_{\alpha} \delta_{\alpha\beta}, \quad (\text{S8})$$

where n_{α} is the occupation number of the state α in the Hartree-Fock calculations, and ε_{α} is the Hartree-Fock quasiparticle energy. We currently work at zero temperature, such that n_{α} is either 1 or 0.

To go beyond the Hartree-Fock calculation and to allow number of electrons to be different from what is set in the Hartree-Fock calculations, we now divide the quasiparticle states into several groups. The first group includes quasiparticle states with quasiparticle energies much lower than the Fermi energy. These states are called frozen states, and all other states are called free states. To facilitate further reasoning, we defined another group of states, called melted states. Melted states includes quasiparticle states with occupation number 1 in the Hartree-Fock calculations but is now allowed to change. Melted states is a subset of free states. Melted states can be empty, for which all the occupied quasiparticle states in the Hartree-Fock calculations are frozen.

The Hilbert space defined above is called the reduced Hilbert space. The simplification is that frozen states are always occupied, which greatly reduces the number of electrons that need to be dealt with. Our ultimate purpose is to derive an effective Hamiltonian in the reduced Hilbert space.

We first look at the kinetic part $\sum_{\alpha, \beta} T_{\alpha\beta} \hat{c}_{\alpha}^{\dagger} \hat{c}_{\beta}$. If both α and β belongs to the frozen states, the term is a constant in the restricted Hilbert space. If one of $\{\alpha, \beta\}$ belongs to the frozen states and the other one belongs to the free states, the term is zero in the restricted Hilbert space. Therefore, the effective kinetic Hamiltonian is

$$H_{\text{eff}}^{\text{kin}} = \sum_{\alpha, \beta \in \text{free}} T_{\alpha\beta} \hat{c}_{\alpha}^{\dagger} \hat{c}_{\beta}. \quad (\text{S9})$$

With the same logic, the effective interaction Hamiltonian is

$$H_{\text{eff}}^{\text{int}} = \frac{1}{2} \sum_{\alpha, \beta, \gamma, \delta \in \text{free}} V_{\alpha\beta\gamma\delta} \hat{c}_{\alpha}^{\dagger} \hat{c}_{\beta}^{\dagger} \hat{c}_{\gamma} \hat{c}_{\delta} + \sum_{\alpha, \beta \in \text{free}; \gamma \in \text{frozen}} (V_{\gamma\alpha\beta\gamma} - V_{\gamma\alpha\gamma\beta}) \hat{c}_{\alpha}^{\dagger} \hat{c}_{\beta}. \quad (\text{S10})$$

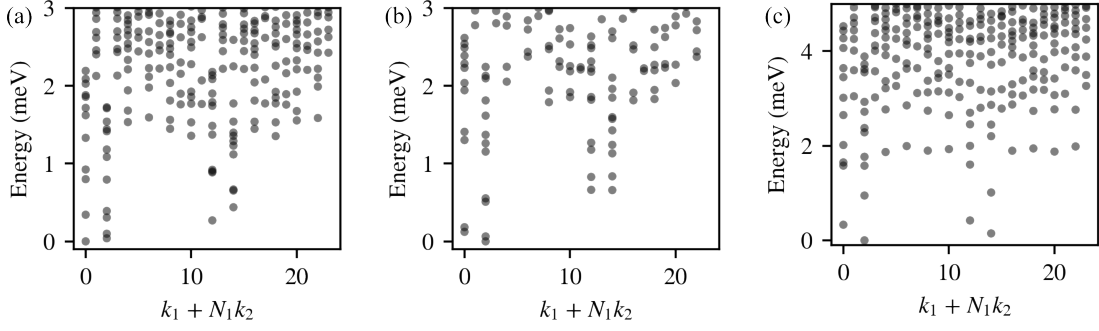


FIG. S2. Many-body spectrum on a 4×6 supercell for tMoTe_2 at twist angle 1.89° [(a)] and 2.14° [(b)]. The ED calculations for (a) and (b) are performed after HF calculations. (c) shows the many-body spectrum of tMoTe_2 at twist angle 2.00° , but with bare DFT bands. For all calculations, the Hilbert space is restricted to the second moiré miniband, which is half-filled. The first moiré miniband is empty. The parameters are the same as that used in the main text.

Together, the effective Hamiltonian is

$$H_{\text{eff}} = \sum_{\alpha, \beta \in \text{free}} \left[T_{\alpha\beta} + \sum_{\gamma \in \text{frozen}} (V_{\gamma\alpha\beta\gamma} - V_{\gamma\alpha\gamma\beta}) \right] \hat{c}_\alpha^\dagger \hat{c}_\beta + \frac{1}{2} \sum_{\alpha, \beta, \gamma, \delta \in \text{free}} V_{\alpha\beta\gamma\delta} \hat{c}_\alpha^\dagger \hat{c}_\beta^\dagger \hat{c}_\gamma \hat{c}_\delta \quad (\text{S11})$$

$$= \sum_{\alpha \in \text{free}} \varepsilon_\alpha \hat{c}_\alpha^\dagger \hat{c}_\alpha + \frac{1}{2} \sum_{\alpha, \beta, \gamma, \delta \in \text{free}} V_{\alpha\beta\gamma\delta} \hat{c}_\alpha^\dagger \hat{c}_\beta^\dagger \hat{c}_\gamma \hat{c}_\delta - \sum_{\alpha, \beta \in \text{free}; \gamma \in \text{melted}} (V_{\gamma\alpha\beta\gamma} - V_{\gamma\alpha\gamma\beta}) \hat{c}_\alpha^\dagger \hat{c}_\beta, \quad (\text{S12})$$

where the last term is the double counting term to be removed.

IV. ADDITIONAL MANY-BODY CALCULATIONS FOR TWISTED BILAYER MOTe_2

A. Many-body spectra supporting the main text

Additional many-body spectrums for tMoTe_2 at various twist angles are shown in Fig. S2. They show (1) absence of non-Abelian states at twist angle 1.89° with ED on top of HF calculations; (2) evidence of non-Abelian states at twist angle 2.14° with ED on top of HF calculations; (3) absence of non-Abelian states at twist angle 2.00° with ED on top of DFT calculations.

We have also performed ED calculations on a 4×3 supercell, the spin gap is 4.32 meV for tMoTe_2 at the twist angle 2.00° . The ED calculation is performed on top of HF calculations and the filling factor is $\nu = -5/2$. Here, the definition of spin gap is defined as the energy difference between the lowest non-fully-valley-polarized state and the full-valley-polarized ground state.

B. Convergence test for number of bands in Hartree-Fock calculations

Hartree-Fock calculations mix Bloch states from different DFT bands. To test whether enough bands have been taken into account in the HF calculations, we include two, three and four bands in the HF calculations and perform ED on top of the HF bands for tMoTe_2 at twist angle 2° . The many-body spectra, presented in Fig. S3, show minimal changes between three-band and four-band calculations, confirming the convergence of the results presented in the main text. Since ED calculations are restricted to the second moiré valence band, the above results also show that the second DFT moiré band mainly receives contribution from the first and the third DFT moiré valence bands.

C. Influence of dielectric constant and the gate-sample distance

We investigate the stability of the non-Abelian state with respect to screening, controlled by the dielectric constant and the gate-sample distance. In Fig. S4, we present the many-body gap as a function of the above two parameters. The range of the gate sample distance is chosen such that it is comparable to the moiré lattice constant ($\sim 100 \text{ \AA}$ at twist angle 2°). The non-Abelian state is suppressed by both types of screening.

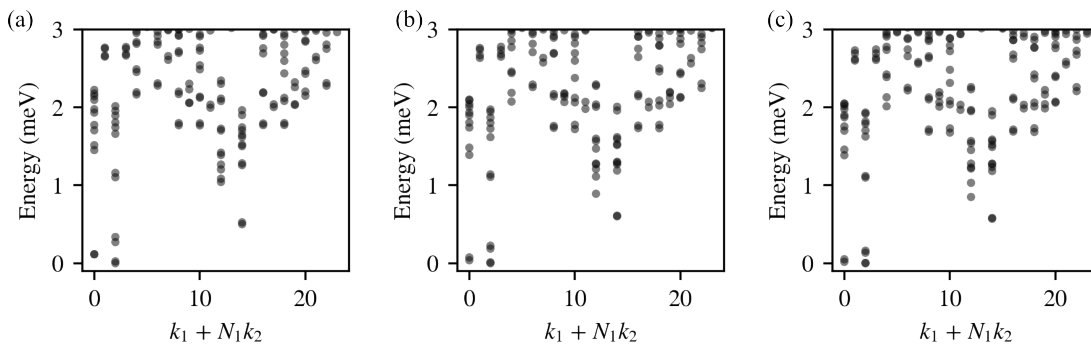


FIG. S3. Many-body spectra on a 4×6 supercell for tMoTe_2 at twist angle 2.00° . Top two [(a)], three [(b)], four [(c)] bands are included in the Hartree-Fock calculations. The parameters are the same as that used in the main text.

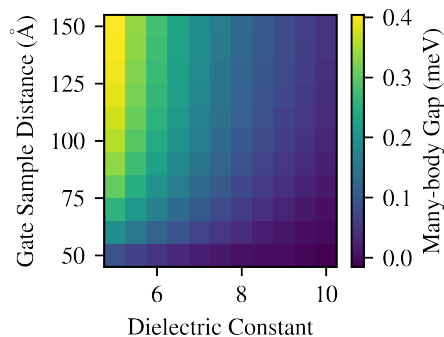


FIG. S4. Many-body gap as a function of dielectric constant and the gate-sample distance. In this figure, the system is in the non-Abelian state for all combinations of parameters. The many-body gap is identified on a 4×6 supercell for tMoTe_2 at twist angle 2.00° .

D. Exact diagonalization calculations with more system sizes

To show that our calculations are robust with respect to system sizes. We perform exact diagonalization on four additional geometry and present the results in Fig. S5. All calculations consistently exhibit six ground states, as expected for systems with an even number of electrons. Furthermore, the spectra for tMoTe_2 closely resemble those of the first Landau level.

V. SIGNATURES OF READ-REZAYI STATE IN TWISTED BILAYER MOTe_2

Given that the second moiré miniband resembles the first LL, it is natural to ask whether the Read-Rezayi state [2] can be realized in tMoTe_2 . In Fig. S6, we present ED spectra for tMoTe_2 at hole filling $\nu = -13/5$ and first LL at electron filling $\nu = 2/5$. The LL system is supposed to be in the Read-Rezayi state.

The ED evidence for the Read-Rezayi state is a 10-fold ground state degeneracy at the sector of zero total momentum for a 5×5 supercell. However, even for the first LL, no obvious gap can be observed between the 10th and the 11th state [Fig. S6(b)], possibly due to finite size effects. The 10-fold degeneracy can be revealed by adding additional screening to the interaction [Fig. S6(d)]:

$$\nu(\mathbf{q}) = \frac{e^2}{2\epsilon_0\epsilon|\mathbf{q}||1 + 6\tanh(|\mathbf{q}|^2 l_B^2/2)/|\mathbf{q}|l_B}}, \quad (\text{S13})$$

where l_B is the magnetic length. The above form of screening comes from virtual excitations of electron-hole pairs in LLs in bilayer graphene [3]. It is not completely reasonable to use this type of screening in the context of tMoTe_2 . Nevertheless, the ED spectrum for tMoTe_2 [Fig. S6(a,c)] resembles that of the LL system [Fig. S6(b,d)] regardless of the choice of $\nu(\mathbf{q})$. Therefore, it is possible that Read-Rezayi state can be realized in tMoTe_2 at zero magnetic field.

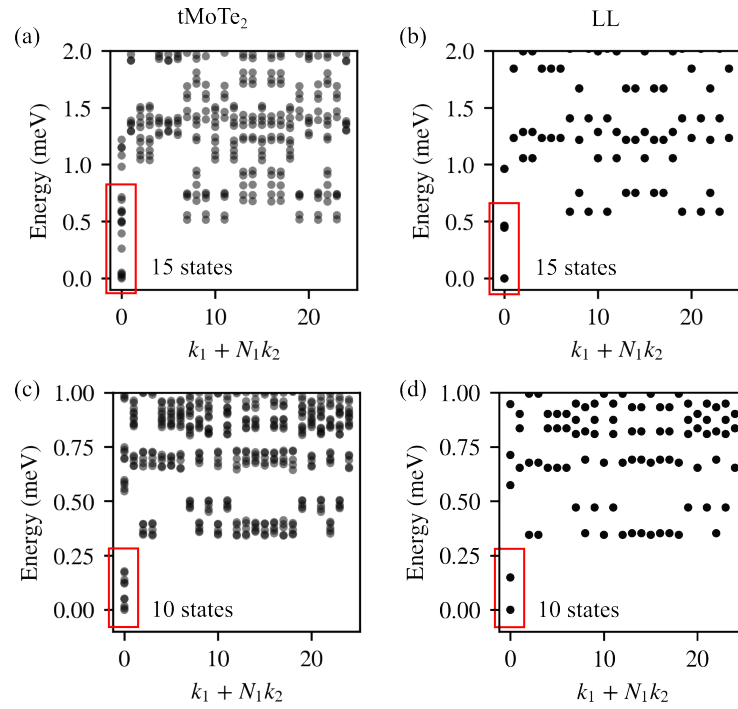
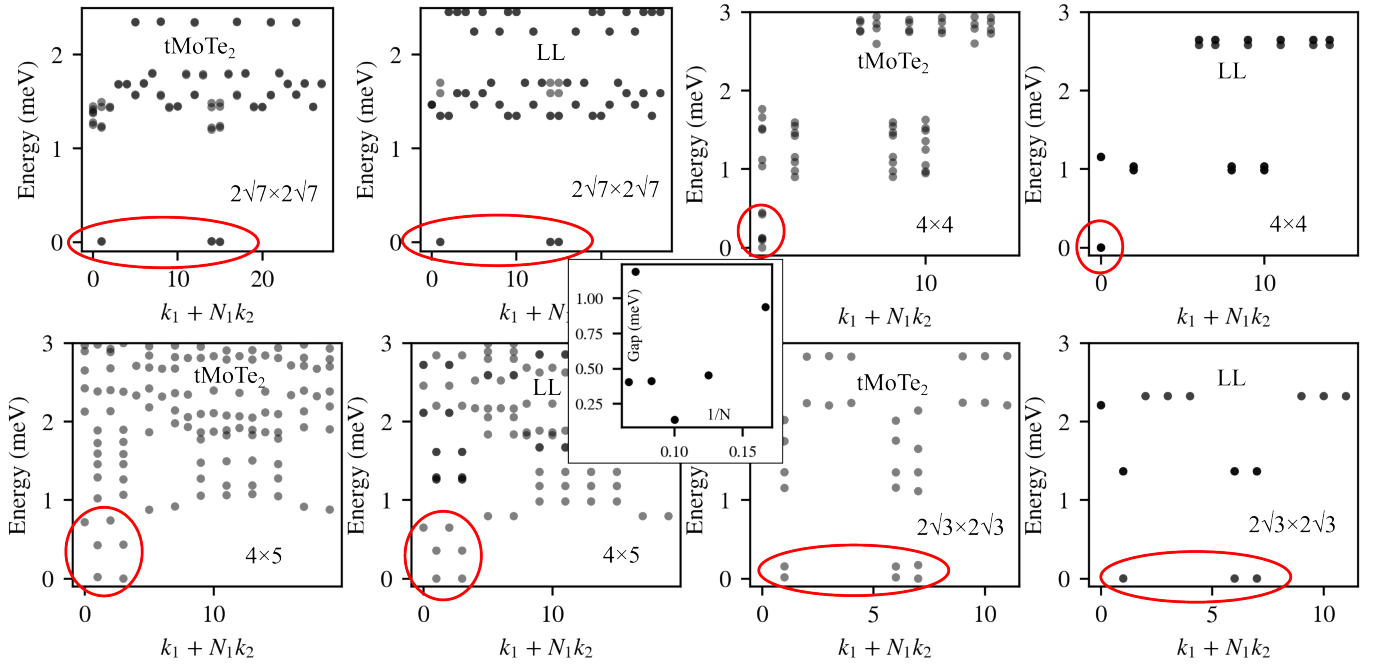


FIG. S6. Many-body spectra for $t\text{MoTe}_2$ (left) and first LL (right) on a 5×5 supercell. The filling for $t\text{MoTe}_2$ is $\nu = -13/5$, and the twist angle is 2.00° . For (a) and (b), the interaction parameters are the same used in the main text. For (c) and (d), additional screening has been included in the calculations.

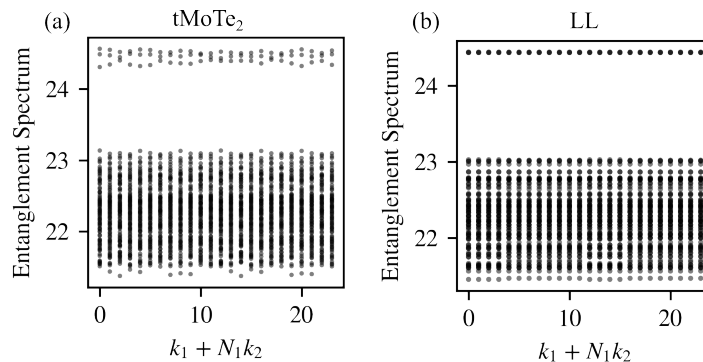


FIG. S7. Particle entanglement spectrum for half-filled tMoTe₂ (left) and first LL (right) on a 4×6 supercell. To calculate the spectrum, the system is broken into two subsystems, with one of the subsystem having 3 particles. The number of levels below the spectrum gap for both (a) and (b) is 1952.

VI. PARTICLE ENTANGLEMENT SPECTRUM FOR NONABELIAN STATES IN TWISTED BILAYER MOTE₂

Generally, to calculate entanglement spectrum, the Hilbert space \mathcal{H} is needed to be decomposed into the tensor product of two different Hilbert spaces:

$$\mathcal{H} = \mathcal{H}_A \otimes \mathcal{H}_B. \quad (\text{S14})$$

For example, a spin chain can be split into two, and the original Hilbert space is the tensor product of the Hilbert spaces associated with the two parts of the spin chain.

However, Hilbert space decomposition by splitting the particles is subtle. To construct such a decomposition, it is necessary to enlarge the Hilbert space. The original Hilbert space of wave functions containing N particles has to be symmetric or antisymmetric with respect to particle permutation. For $N = N_A + N_B$, we enlarge the Hilbert space to be spanned by $\varphi_\alpha(\mathbf{r}_1, \mathbf{r}_2, \dots, \mathbf{r}_{N_A})\varphi_\beta(\mathbf{r}_{N_A+1}, \mathbf{r}_{N_A+2}, \dots, \mathbf{r}_{N_A+N_B})$, where α (β) labels a basis where N_A (N_B) particles occupy the original orbitals. Notice that for $\varphi_\alpha(\mathbf{r}_1, \mathbf{r}_2, \dots, \mathbf{r}_{N_A})$ and $\varphi_\beta(\mathbf{r}_{N_A+1}, \mathbf{r}_{N_A+2}, \dots, \mathbf{r}_{N_A+N_B})$, we still require particle permutation symmetry or antisymmetry. The above enlargement of the Hilbert space corresponds to dividing the particles into two species, with N_A particles belonging to one species and N_B particles belonging to the other species. Particles from different species are distinguishable.

As an example, we work with four fermions, with $N = 4$ and $N_A = N_B = 2$. A common basis for the original (not enlarged) Hilbert space is the Slater determinant, which can be decomposed with generalized Laplace expansion

$$\begin{aligned} \begin{vmatrix} \phi_1(\mathbf{r}_1) & \phi_2(\mathbf{r}_1) & \phi_3(\mathbf{r}_1) & \phi_4(\mathbf{r}_1) \\ \phi_1(\mathbf{r}_2) & \phi_2(\mathbf{r}_2) & \phi_3(\mathbf{r}_2) & \phi_4(\mathbf{r}_2) \\ \phi_1(\mathbf{r}_3) & \phi_2(\mathbf{r}_3) & \phi_3(\mathbf{r}_3) & \phi_4(\mathbf{r}_3) \\ \phi_1(\mathbf{r}_4) & \phi_2(\mathbf{r}_4) & \phi_3(\mathbf{r}_4) & \phi_4(\mathbf{r}_4) \end{vmatrix} &= \begin{vmatrix} \phi_1(\mathbf{r}_1) & \phi_2(\mathbf{r}_1) \\ \phi_1(\mathbf{r}_2) & \phi_2(\mathbf{r}_2) \end{vmatrix} \begin{vmatrix} \phi_3(\mathbf{r}_3) & \phi_4(\mathbf{r}_3) \\ \phi_3(\mathbf{r}_4) & \phi_4(\mathbf{r}_4) \end{vmatrix} - \begin{vmatrix} \phi_1(\mathbf{r}_1) & \phi_3(\mathbf{r}_1) \\ \phi_1(\mathbf{r}_2) & \phi_3(\mathbf{r}_2) \end{vmatrix} \begin{vmatrix} \phi_2(\mathbf{r}_3) & \phi_4(\mathbf{r}_3) \\ \phi_2(\mathbf{r}_4) & \phi_4(\mathbf{r}_4) \end{vmatrix} \\ &+ \begin{vmatrix} \phi_1(\mathbf{r}_1) & \phi_4(\mathbf{r}_1) \\ \phi_1(\mathbf{r}_2) & \phi_4(\mathbf{r}_2) \end{vmatrix} \begin{vmatrix} \phi_2(\mathbf{r}_3) & \phi_3(\mathbf{r}_3) \\ \phi_2(\mathbf{r}_4) & \phi_3(\mathbf{r}_4) \end{vmatrix} + \dots \end{aligned}$$

The above equation directly specifies how a Slater determinant should be decomposed in the enlarged Hilbert space.

In Fig. S7, we show the particle entanglement spectrum for half-filled tMoTe₂ and first LL. Both show 1952 levels below the spectrum gap, which corresponds to the number of quasihole excitations in the two systems.

-
- [1] L. Chen, T. Mazaheri, A. Seidel, and X. Tang, The impossibility of exactly flat non-trivial Chern bands in strictly local periodic tight binding models, *J. Phys. A* **47**, 152001 (2014).
 - [2] N. Read and E. Rezayi, Beyond paired quantum Hall states: Parafermions and incompressible states in the first excited landau level, *Phys. Rev. B* **59**, 8084 (1999).
 - [3] Z. Papić and D. A. Abanin, Topological phases in the zeroth Landau level of bilayer graphene, *Phys. Rev. Lett.* **112**, 046602 (2014).